

Highlights

Piecewise-analytical evaluation of a class of integrals appearing in the weak turbulence theory of plasma

Brent Page

- Splines enable computation of weak turbulence integrals
- Branch cuts must be monitored when an integral is manipulated into a dilogarithm
- Weak turbulence numerical simulations yield wave spectra with smooth time evolution

Piecewise-analytical evaluation of a class of integrals appearing in the weak turbulence theory of plasma

Brent Page

Berkeley, CA, USA

Abstract

Kinetic plasma instability analyses are often conducted using quasilinear theory despite the existence of the more accurate weak turbulence (WT) theory. This is attributable to the complexity of the WT equations, which currently prevents predictive analysis of them in most contexts. This study presents a program that can determine the effect of one interaction in the WT framework on the development of instabilities. In particular, the program computes an integral that describes induced scattering, a wave-wave-particle interaction. This integral can be evaluated piecewise-analytically when all physical quantities involved, such as the wave dispersion relation and spectral density, are represented using splines. Applied to measurements of a whistler wave spectrum in the solar wind, the program indicates that the time evolution of the spectrum features a transfer of wave power toward smaller wavenumbers. This is consistent with the measurements, but the program overpredicts the amplitude to which the waves grow. This discrepancy can possibly be resolved by future extension of the program to terms in the WT equations that describe three-wave processes, which can be computed using the same methods as those utilized for induced scattering.

Keywords: kinetic plasma, weak turbulence, spline, dilogarithm

1. Introduction

The weak turbulence description of plasma can be used to interpret several heliospheric observations. For example, Langmuir waves in this description scatter on ions to produce electromagnetic radiation at the plasma frequency, explaining the origin of type III solar radio bursts [e.g., 1, 2, 3]. Applied to lower hybrid waves in the magnetosphere, weak turbulence theory predicts an extended lifetime for the associated ion ring distributions as a result of wave-wave-particle interactions that stabilize the wave spectrum [4]. In the solar wind, the steepening of the Alfvén wave spectrum between the inertial and dissipation ranges may also be a consequence of wave-wave-particle interactions [5].

Despite the widespread applicability of the weak turbulence equations, a systematic solver of them is not available due to their complexity. Typically, a number of simplifying assumptions are adopted to make the equations manageable. Non-thermal velocity distribution function (vdf) features are represented using delta functions [e.g., 1, 4]. The linear dispersion relations for the waves are taken to have forms applicable for Maxwellian vdfs [e.g., 2, 3]. The various wave frequencies and their differences are considered in limits that simplify the nonlinear wave-particle

resonances [e.g., 3, 5]. Agreement can be found between observations and the predictions of these simplified weak turbulence equations, but a systematic solver of the exact equations would enable more definitive analyses.

Progress towards this goal has been made for electrostatic spectra and Maxwellian vdfs. A natural starting point in this setting is the plasma dispersion function [6]. The velocity integrals for the weak turbulence equations can be expressed in terms of infinite series involving derivatives of the plasma dispersion function as well as Hermite polynomials [7, 8]. For computation of nonlinear wave growth rates, the resulting so-called quadratic response functions would have to be integrated over wavenumber, which would likely introduce additional complexity. Also, this approach cannot accommodate deviations of the particle vdfs from Maxwellians, which prevents accurate analysis in some contexts.

An alternative starting point is exhibited by the linear solver LEOPARD [9], which replaces the plasma dispersion function with piecewise-analytical integration of spline representations of particle vdfs. The flexibility of this approach is demonstrated by its viability for the several types of velocity integrals involved in the linear analysis of waves in magnetized plasma. At the next level approximation, quasilinear analyses in addition require an integral over wavenumber. Spline representations for the relevant wavenumber-dependent quantities, namely the wave spectral density and dispersion relation, again lead to piecewise-analytical expressions [10].

The weak turbulence equations for waves propagating parallel to a background magnetic field can also be programmed using this integration strategy. Even with this wavevector restriction, these equations are rather complicated and have only been derived relatively recently [11]. For several reasons, this paper is further restricted to the induced scattering term that involves two electromagnetic waves and a particle. This term only requires a double integral over wavenumber and velocity, while those describing three-wave processes require triple integrals. Also, as argued in Sect. 4, among the nonlinear processes in the weak turbulence description, induced scattering plausibly has a relatively strong influence on the evolution of whistler wave spectra. Broadband spectra of parallel-propagating whistlers are commonly observed in the solar wind [e.g., 12, 13] and evolve on timescales that can be measured by a single spacecraft, so are an ideal subject for a weak turbulence analysis.

A Fortran program, *fort-kv-ints*, that computes a general form of the induced scattering double integral is outlined in Sect. 2. A validation of *fort-kv-ints* is described in Sect. 3. Measurements of a solar wind whistler wave event are presented in Sect. 4. LEOPARD and *fort-kv-ints* are used to compute the linear growth rate as well as the nonlinear growth rate attributable to induced scattering for this event, and the predicted evolution in the spectrum is compared with the measurements. Alongside a summary, the conclusion section includes a discussion of the computations required for extending the program to three-wave interactions.

2. Methods

2.1. Target expression

For right-handed circularly polarized electromagnetic waves with a magnetic field spectral density $I_+^B(k)$ propagating along the background magnetic field \vec{B}_0 in a plasma with an electron velocity distribution function $F(v_{\parallel}, v_{\perp})$ and immobile charge-neutralizing ions, Appendix A

shows that induced scattering introduces a nonlinear growth rate

$$\begin{aligned} \gamma_k^{nl} = & -\frac{\pi}{\delta^2 \tilde{\omega}_k^+ \tilde{\Lambda}_{K_+}^+} \text{Im} \left[i \int d\tilde{k}' \left(\frac{\tilde{\omega}_{k'}^+}{\tilde{k}'} \right)^2 \int d\tilde{v}_\perp d\tilde{v}_\parallel \tilde{v}_\perp^2 \tilde{g}_{K_+}^{-1} \tilde{T}_{K_+} \tilde{g}_{K_+ - K_+'}^0 [(\tilde{T}_{-K_+} - \tilde{D}_{-K_+}) \tilde{g}_{K_+}^{-1} \tilde{T}_{K_+} + \right. \\ & \left. (\tilde{T}_{K_+} - \tilde{D}_{K_+}) \tilde{g}_{-K_+}^{-1} \tilde{T}_{-K_+}] \tilde{F}(\tilde{v}_\parallel, \tilde{v}_\perp) \tilde{I}_+^B(\tilde{k}') \right], \end{aligned} \quad (1)$$

where

$$\begin{aligned} \tilde{T}_K &= -i \left(\frac{\tilde{\omega} - \tilde{k} \tilde{v}_\parallel}{\tilde{\omega}} \frac{\partial}{\partial \tilde{v}_\perp} + \frac{\tilde{k} \tilde{v}_\perp}{\tilde{\omega}} \frac{\partial}{\partial \tilde{v}_\parallel} \right), \\ \tilde{D}_K &= i \frac{\tilde{\omega} - \tilde{k} \tilde{v}_\parallel}{\tilde{\omega}} \frac{1}{\tilde{v}_\perp}, \\ \tilde{g}_K^M &= \frac{1}{\tilde{\omega} - \tilde{k} \tilde{v}_\parallel + M + i\epsilon}, \\ \Lambda_K^+ &= 1 + \frac{\pi i}{\delta^2 \tilde{\omega}} \int d\tilde{v}_\perp d\tilde{v}_\parallel \tilde{v}_\perp^2 \tilde{g}_K^{-1} \tilde{T}_K \tilde{F}(\tilde{v}_\parallel, \tilde{v}_\perp) - \frac{\tilde{k}^2}{\tilde{\omega}^2 \delta^2}, \\ \tilde{\Lambda}_{K_+}^+ &= \frac{1}{|\Omega_{ce}|} \left. \frac{\partial \text{Re } \Lambda_K^+}{\partial \tilde{\omega}} \right|_{\tilde{\omega}=\tilde{\omega}_k^+}, \end{aligned}$$

K is shorthand for $(\tilde{k}, \tilde{\omega})$, the linear dispersion relation $\Lambda_{k, \tilde{\omega}}^+ = 0$ is solved by $\tilde{\omega} = \tilde{\omega}_k^+$, and K_+ is shorthand for $(\tilde{k}, \tilde{\omega}_k^+)$. Also, $i\epsilon$ is an infinitesimal imaginary part. In addition, the frequency $\omega = \tilde{\omega} |\Omega_{ce}|$ and growth rate $\gamma_k^{nl} = \tilde{\gamma}_k^{nl} |\Omega_{ce}|$ are normalized by the absolute value $|\Omega_{ce}|$ of the electron angular gyrofrequency $\Omega_{ce} = eB_0/(m_e c)$, where $e = -|e|$ is the electron charge, m_e is the electron mass, c is the speed of light, and B_0 is the magnitude of the background magnetic field; wavenumber $k = \tilde{k} \omega_{pe}/c$ is normalized by the inverse electron inertial length ω_{pe}/c , where $\omega_{pe} = \sqrt{4\pi e^2 n_e/m_e}$ is the electron plasma frequency and n_e is the electron density; velocity parallel $v_\parallel = \tilde{v}_\parallel v_{A,e}$ and perpendicular $v_\perp = \tilde{v}_\perp v_{A,e}$ to \vec{B}_0 are normalized by the electron Alfvén speed $v_{A,e} = c|\Omega_{ce}|/\omega_{pe}$; and $\delta \equiv |\Omega_{ce}|/\omega_{pe}$. Also, $\int d\tilde{v}_\parallel \int d\tilde{v}_\perp 2\pi \tilde{v}_\perp \tilde{F}(\tilde{v}_\parallel, \tilde{v}_\perp) = 1$. Lastly, the magnetic field spectral density $\tilde{I}_+^B(\tilde{k})$ satisfies $2 \int_{-\infty}^{\infty} d\tilde{k} \tilde{I}_+^B(\tilde{k}) = \langle |\vec{B}(z, t)|^2 \rangle / B_0^2$, where $\vec{B}(z, t)$ is the wave magnetic field as a function of position z and time t , and the angular brackets denote an ensemble average.

2.2. Decomposition of velocity integrals

With the vdf $F(v_\parallel, v_\perp)$, spectral density $I_+^B(k)$, and dispersion relation $\omega(k) = \omega_k^+$ represented using splines, the computationally challenging portion of Eq. (1) is

$$\mathcal{I} \equiv \int dk \int dv_\parallel \frac{k^q v_\parallel^n}{t_1^{l_1} t_2^{l_2} t_3^{l_3}}, \quad (2)$$

where

$$\begin{aligned} t_1 &\equiv \omega_1 - k_1 v_\parallel - 1 + i\epsilon, \\ t_2 &\equiv -\omega(k) + k v_\parallel + 1 + i\epsilon, \end{aligned}$$

$$t_3 \equiv \omega_1 - \omega(k) - (k_1 - k)v_{\parallel} + i\epsilon,$$

$\omega_1 \equiv \omega(k_1)$, and all tildes have been dropped.

As a first reduction step, partial fraction decomposition is used to express these integrals in terms of, e.g.,

$$\int dk \frac{1}{[h(k)]^\sigma} \int dv_{\parallel} \frac{k^q v_{\parallel}^n}{(v_{\parallel} - (\omega(k) + 1 + i\epsilon)/k)^{\lambda_2}} \quad (3)$$

and similar integrals involving the other denominator terms t_1 and t_3 of Eq. (2), all having the same new term $h(k) \equiv k\omega_1 - k_1\omega(k) + k_1 - k$. Also, computation of Eq. (2) for given powers $\lambda_m = \lambda'_m$ requires computation of Eq. (3) for powers $\lambda_2 = 0 \dots \lambda'_2$ and $\sigma = 0 \dots (\lambda'_1 + \lambda'_3)$.

If $n = 0$ in Eq. (3), the velocity integral can be done in one step. If $\lambda_2 > 1$, this yields a rational integral over k for each velocity bound. The $\lambda_2 = 1$ case produces k integrals that require, following partial fraction expansion, straightforward integration by parts in some cases and, as addressed in Sect. 2.3, use of a special function in others.

The reduction rule

$$\frac{v_{\parallel}}{v_{\parallel} - (\omega(k) + 1)/k} = 1 + \frac{(\omega(k) + 1)/k}{v_{\parallel} - (\omega(k) + 1)/k} \quad (4)$$

can be used to express the $n = n'$ cases of Eq. (3) in terms of $n = n' - 1$ cases. If $\omega(k)$ is represented using a quadratic spline, then Eq. (4) shows that calculation of Eq. (3) for given $q = q'$ and $n = n'$ requires that the $n = n' - 1$ cases be computed for $q = q' - 1$ and $q = q' + 1$. By extension, the $n = 0$ base case must be done for q from $q = q' - n$ to $q = q' + n$. If a quintic spline is used to represent the vdf, then it is necessary to compute Eq. (3) for powers of v_{\parallel} as high as $n = 8$, meaning the $n = 0$ case must be computed for powers of k at least as extreme as $-8 \leq q \leq 8$. In fact, recombination of the sub-integrals like Eq. (3) into the complete integral Eq. (2) also requires supplemental factors of k . In full, decomposition of Eq. (2) produces simpler integrals that must be evaluated for powers of k that are more demanding than those needed for Eq. (2) by as much as $-10 \leq \Delta q \leq 30$.

2.3. Dilogarithm integrals

The only special function used in fort-kv-ints is the dilogarithm [14]

$$\text{Li}_2(z) \equiv - \int_0^z \frac{\ln(1-t)}{t} dt,$$

which arises in the computation of integrals of the form

$$\int^{k_b} dk \frac{1}{k - k_r} \int^{v_{\parallel,b}} dv_{\parallel} \frac{1}{v_{\parallel} - p(k)}, \quad (5)$$

where $p(k)$ can be taken to be a polynomial function of k for purposes of illustration. After some elementary operations, Eq. (5) becomes a sum of several integrals with the form

$$\int^{k_b} dk \frac{1}{k - k_r} \ln(k - k_j(v_{\parallel,b})) \quad (6)$$

where $k_j(v_{\parallel,b})$ is a root of $v_{\parallel,b} - p(k)$. Also, $k_j(v_{\parallel,b})$ and k_r are complex-valued.

The integral in Eq. (6) can be expressed as a sum of a dilogarithm and elementary functions, but this involves manipulations of $\ln()$ that must be handled with care. In terms of $\xi \equiv k - k_r$, Eq. (6) becomes

$$\int^{k_b - k_r} d\xi \frac{1}{\xi} \ln(\xi + k_r - k_j(v_b)). \quad (7)$$

Further progress requires splitting the \ln into $\ln(k_r - k_j(v_{\parallel,b})) + \ln(1 - \xi/(k_j(v_{\parallel,b}) - k_r))$, which may require a correction term $\pm 2\pi i$ depending on the \ln arguments. In particular,

$$\ln(\xi + k_r - k_j(v_{\parallel,b})) = \ln(k_r - k_j(v_{\parallel,b})) + \ln\left(1 - \frac{\xi}{k_j(v_{\parallel,b}) - k_r}\right) + 2\pi i N(\xi, v_{\parallel,b})$$

where

$$N(\xi, v_{\parallel,b}) = \begin{cases} +1 & s < -\pi \\ -1 & s > \pi \\ 0 & \text{else} \end{cases} \quad (8)$$

with

$$s \equiv \text{Arg}(k_r - k_j(v_{\parallel,b})) + \text{Arg}\left(1 - \frac{\xi}{k_j(v_{\parallel,b}) - k_r}\right),$$

so Eq. (7) becomes

$$\int^{k_b - k_r} d\xi \frac{1}{\xi} \left[\ln(k_r - k_j(v_{\parallel,b})) + \ln\left(1 - \frac{\xi}{k_j(v_{\parallel,b}) - k_r}\right) + 2\pi i N(\xi, v_{\parallel,b}) \right], \quad (9)$$

$$= \ln(k_r - k_j(v_{\parallel,b})) \ln(k_b - k_r) - \text{Li}_2\left(\frac{k_b - k_r}{k_j(v_{\parallel,b}) - k_r}\right) + 2\pi i \int^{k_b - k_r} d\xi \frac{1}{\xi} N(\xi, v_{\parallel,b}). \quad (10)$$

If $N(\xi, v_{\parallel,b})$ does not change as a function of ξ , then the condition in Eq. (8) can simply be evaluated for each velocity endpoint $v_{\parallel,b}$ and the split \ln correction integral $2\pi i N(v_{\parallel,b}) \ln(k_b - k_r)$ included in Eq. (10) as appropriate. A more complicated treatment is required if $N(\xi, v_{\parallel,b})$ varies with ξ . Such variation takes the form of a ± 1 discontinuity, which arises from the \ln argument $\eta \equiv 1 - \xi/(k_j(v_{\parallel,b}) - k_r)$ in Eq. (9) crossing the negative real axis. Setting $\text{Im}(\eta) = 0$ and solving for k yields a single solution $k_c = \text{Im}(k_j(v_{\parallel,b})k_r^*)/\text{Im}(k_j(v_b) - k_r)$ for this crossing point. If $\text{Re}(\eta) < 0$ at $k = k_c$, then $N(k - k_r, v_{\parallel,b})$ changes from ± 1 to 0 at $k = k_c$. The definite integral with lower k_ℓ and upper k_u bounds spanning k_c then requires a split \ln correction $\pm 2\pi i N(k_{u/\ell} - k_r, v_{\parallel,b}) [\ln(k_{u/\ell} - k_r) - \ln(k_c - k_r)]$, where this expression is evaluated at the bound $k_{u/\ell}$ at which $N(k_{u/\ell} - k_r, v_{\parallel,b}) \neq 0$, and the leading $+$ and $-$ signs apply for the k_u and k_ℓ bounds, respectively. For all other intervals, the correction is $2\pi i N(k_b - k_r, v_{\parallel,b}) [\ln(k_u - k_r) - \ln(k_\ell - k_r)]$, where k_b can be either k_u or k_ℓ .

3. Validation

The computation of Eq. (2) by fort-kv-ints has been validated using multiple methods. For k and v_{\parallel} intervals for which the denominator terms t_1 , t_2 , and t_3 do not pass through $t_m = i\epsilon$, numerical integration tools can be utilized to obtain reference calculations of Eq. (2). Confirming that they agree with corresponding results from fort-kv-ints does not conclusively validate the program because the behavior of the integrand in Eq. (2) is extremely altered at the resonant

Table 1: Comparison of fort-kv-ints and Mathematica results for a non-resonant integral that requires enhanced working precision.

$v_{\parallel,\ell} = 2.2$	$v_{\parallel,u} = 2.3$
$k_\ell = 0.11$	$k_u = 0.12$
$k_1 = 0.124$	$\omega_1 = 0.0147$
$\omega(k)^1 = -0.002 + (0.132)k + (0.015)k^2$	
$q = 6$	$n = 6$
$\lambda_1 = 1$	$\lambda_2 = 2 \quad \lambda_3 = 2$
$\text{Re}(\mathcal{I}_{f,54})^2$	6×10^4
$\text{Re}(\mathcal{I}_{f,72})^3$	$-6.883824890 \times 10^{-4}$
$\text{Re}(\mathcal{I}_M)^4$	$-6.883824895 \times 10^{-4}$

¹ Spline representation of the dispersion relation for the interval $k_\ell < k < k_u$

² fort-kv-ints with 54 digits of working precision

³ fort-kv-ints with 72 digits of working precision

⁴ Mathematica numerical integration

points $t_m = i\epsilon$. However, this exercise still serves as an effective probe for bugs because the integrals that include resonant points are computed using the same code as those that do not.

Table 1 reports calculations of Eq. (2) from both fort-kv-ints \mathcal{I}_f and Mathematica \mathcal{I}_M for one possible set of integral parameters. If the working precision of fort-kv-ints is set to 72 digits, the program agrees with Mathematica; $\text{Re}(\mathcal{I}_{f,72}) = \text{Re}(\mathcal{I}_M)$ with 9 digits of consistency. However, when the precision is reduced to 54 digits, fort-kv-ints becomes incorrect; $\text{Re}(\mathcal{I}_{f,54}) \neq \text{Re}(\mathcal{I}_M)$.

The source of this error can be traced to the stage of fort-kv-ints that computes integrals over rational functions of wavenumber. For reasons outlined in Sect. 2, these feature powers of k as high as $q = 25$ for the integral addressed in Table 1. The poles of the rational functions include the roots k_α and k_β of the denominator term $t_2(v_{\parallel,b}) = -\omega(k) + kv_{\parallel,b} + 1 + i\epsilon = c(k - k_\alpha)(k - k_\beta)$ appearing in Eq. (2), where $v_{\parallel,b}$ is a bound of the velocity integral and c is the quadratic coefficient of $t_2(v_{\parallel,b})$. For the parameters in Table 1, $k_\alpha \approx 140$ and $k_\beta \approx -0.5$. Part of the partial fraction expansion of these rational functions operates on $k^q/(k - k_\alpha)$, which produces a term with size k_α^{q-1} [e.g., 15]. For $q = 25$, this corresponds to $k_\alpha^{q-1} \sim 10^{52}$. As a consequence, reproducing the result $\mathcal{I}_M \sim -7 \times 10^{-4}$ from Mathematica indicated in Table 1 requires arithmetic that involves cancellation of more than 56 digits. This explains the failure of fort-kv-ints when only 54 digits are used.

Tests of fort-kv-ints similar to that described in Table 1 have been conducted for a set of integral parameters designed to encompass all use cases of the program. To be specific, as mentioned above, this test suite is comprehensive apart from the exclusion of integrals that include a resonance $t_m = i\epsilon$, which cannot be estimated to arbitrary accuracy using Mathematica numerical integration. For all tests in this nearly comprehensive set, a target of 9 digits of consistency between fort-kv-ints and Mathematica has been attained. This provides a strong indication that fort-kv-ints correctly computes Eq. (2) for non-resonant cases.

In general, identifying the required working precision level for a given integral involves trial and error combined with an analysis of its parameters similar to that described above. A reliable indicator that the adopted number of digits is adequate is invariance of the program result as the number is increased. For the application described in Sect. 4, which involves evaluation of Eq.

(2) for several thousand sets of parameters, 108 digits were found to be sufficient.

Table 2: Comparison of k -first and v_{\parallel} -first computations of Eq. (2) that involve a resonant point $t_1 = i\epsilon$. Integral results are stated up to the first digit of disagreement.

$v_{\parallel,l} = -5.05$		$v_{\parallel,u} = -4.96$	$k_l = 0.27$	$k_u = 0.28$
$k_1 = 0.1$		$\omega_1 = 0.5$	$\omega(k) = 0.14 + (1.1)k$	
$q = 5$		$n = 5$		
		$\lambda_1 = 3$	$\lambda_2 = 0$	$\lambda_3 = 2$
$\text{Re}(I)$	k -first	$-0.6384400132846682596235 \times 10^4$		
	v_{\parallel} -first	$-0.6384400132846682596236 \times 10^4$		
$\text{Im}(I)$	k -first	25.2664378606151		
	v_{\parallel} -first	25.2664378606153		

When computing Eq. (2), fort-kv-ints integrates v_{\parallel} first, k second. A k -first version can be developed that uses the same core subroutines but that calls them with different arguments and that features substantial alterations to the overall program structure. For example, in the k -first version, initial reduction steps analogous to those in Sect. 2 produce different reduced rational functions than those, e.g., in Eq. (3), that arise in the v_{\parallel} -first version. Due to such differences, the probability of k -first and v_{\parallel} -first implementations producing the same incorrect result is negligible. As a result, confirming agreement between these two calculations can validate both. These tests also notably can be conducted for both resonant and non-resonant integrals. However, with $\omega(k)$ represented using an order s spline, k -first piecewise-analytical integration of Eq. (2) is prohibitively difficult for $s > 1$. For this reason, this intervalation is limited to $s = 1$.

Comparisons of k -first and v_{\parallel} -first computations have been conducted for a range of parameters designed to cover all program use cases, and a representative example is described in Table 2. The ω , k , and v_{\parallel} parameters stated here lead to a resonant point $t_1 = i\epsilon$ at $v_{\parallel} = (\omega_1 - 1)/k_1 = -5.0$. Using 35 digits of working precision, the k -first and v_{\parallel} -first computations feature at least 15 digits of agreement in both their real and imaginary parts. Other classes of use cases that have been tested include integrals with resonant points $t_2 = i\epsilon$ and $t_3 = i\epsilon$, which feature similar levels of agreement. Combined with the validation of the non-resonant integrals described above, the success of these tests provides confidence in the accuracy of fort-kv-ints.

4. Application

4.1. Whistler event

Whistler waves are electromagnetic waves that propagate in magnetized plasma at frequencies f less than the electron gyrofrequency $f_{ce} = |\Omega_{ce}|/(2\pi)$ and much greater than the proton gyrofrequency [16]. For the specific case of propagation along the background field \vec{B}_0 , the electric and magnetic fields of a whistler rotate in time in concert with electrons in a right-handed sense about \vec{B}_0 . Assuming $\omega_{pe} \gg |\Omega_{ce}|$, proton motion can be ignored for parallel-propagating whistlers at frequencies above $f \sim 0.01f_{ce}$ [17].

In the solar wind, fairly steady-state whistler spectra are observed accompanying linearly unstable electron vdfs. Figures 1 and 2 show an example of such a set of observations by the ARTEMIS spacecraft [18]. This is a snapshot of a longer whistler event that has been previously analyzed in [19]. The dynamic magnetic field spectrum $P_B(t, f)$ in the top panel of Fig. 1,

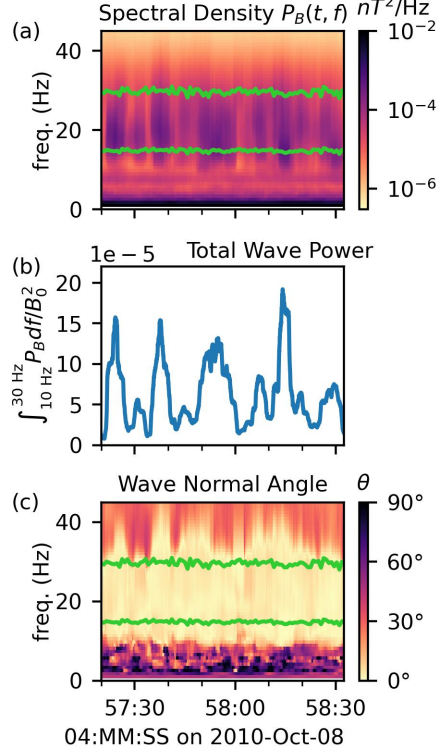


Figure 1: Magnetic field measurements from the ARTEMIS P2 spacecraft of a whistler wave event in the solar wind over a $\Delta t \approx 1$ minute timespan. The dynamic spectrum in panel (a) shows a band of wave power approximately bounded by $\approx 0.1f_{ce}$ and $\approx 0.2f_{ce}$, which are marked with green lines. Panel (b) presents the total wave power, highlighting bursts that are interspersed with periods of relatively weaker wave activity. During the weaker periods, e.g., from 04:57:40 to 04:57:50, the dynamic spectrum remains heightened in the whistler band, indicating that these waves retain a finite amplitude. Panel (c) displays the wave propagation angle with respect to \vec{B}_0 , showing it to be $\theta \approx 0^\circ$.

derived from search coil magnetometer (SCM) measurements [20], contains a band of wave power between roughly $f = 10$ Hz and $f = 30$ Hz persisting over the full $\Delta t \approx 1$ minute time interval that is presented. The background magnetic field, measured by a fluxgate magnetometer [21], has magnitude $B_0 \approx 5$ nT. This corresponds to $f_{ce} \approx 140$ Hz, so the observed wave power lies in the whistler range, $0.1f_{ce} \lesssim f \lesssim 0.2f_{ce}$.

The spectral density $P_B(t, f)$ in Fig. 1(a) has been constructed such that $\int_0^{64 \text{ Hz}} P_B(t, f) df = \langle |\vec{B}[n]|^2 \rangle$, where the right hand side is the mean-squared magnitude of the magnetic field $\vec{B}[n]$ in the SCM data series, n is a time index, and 64 Hz is the Nyquist frequency for these measurements. Figure 1(b) shows an estimate of the mean-squared magnitude $\mathfrak{B}_{emp.} \equiv \int_{10 \text{ Hz}}^{30 \text{ Hz}} P_B(t, f) df / B_0^2$ of the fluctuating magnetic field in the whistler band, normalized by the squared magnitude of the background magnetic field. Averaged over the full $\Delta t = 1$ minute interval, $\overline{\mathfrak{B}_{emp.}} \approx 6 \times 10^{-5}$. This establishes that the whistler wave field can be considered a small perturbation relative to \vec{B}_0 , partly justifying use of the weak turbulence expansion for analysis of this event. On the other hand, the variation in $\mathfrak{B}_{emp.}$ seen in Fig. 1(b) indicates that the whistler spectrum is influenced by

dynamics operating on timescales $\Delta t \gtrsim 10$ s much longer than the longest whistler wave period. Optimally, an analysis could be conducted on subintervals of this figure, e.g., from 04:57:50 to 04:57:55, over which $\mathfrak{B}_{emp.}$ is nearly constant. However, the electron vdf measurements must be averaged in time over a longer interval to ensure that they are sufficiently precise. Selection of the interval shown in Fig. 1 balances these motivations to minimize time variation in the wave spectrum while maximizing the interval duration.

Figure 1(c) presents the wave propagation direction, which is estimated using singular value decomposition [22] of the magnetic field spectral matrices. These computations indicate that the waves propagate parallel or antiparallel to \vec{B}_0 . Inspection of the phase relationship between the wave electric [23] and magnetic fields further constrains this propagation direction to be antiparallel to \vec{B}_0 .

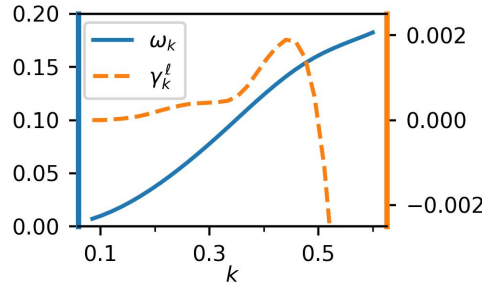


Figure 2: Based off a linear instability analysis of electron vdf measurements, the frequency ω_k and growth rate γ_k^ℓ of waves that propagate antiparallel to the background magnetic field for the event presented in Fig. 1. These quantities are normalized by $|\Omega_{ce}|$, and wavenumber k is normalized by ω_{pe}/c .

An analysis of the electron vdf using a kinetic dispersion solver such as LEOPARD [9] can indicate whether the waves are linearly unstable. Methods adopted to prepare electrostatic analyzer data from ARTEMIS [24] into an electron vdf compatible with LEOPARD are described in [25]. Figure 2 shows this solver's result for the dispersion relation of waves propagating antiparallel to \vec{B}_0 . These waves are found to be linearly unstable, most so at frequencies $\omega \approx 0.15|\Omega_{ce}|$. This appears to align favorably with the observations in Fig. 1, but a 30–50% discrepancy arises between the frequencies of maximum linear instability and maximum empirical wave power when Doppler shifting is taken into account, as shown at the end of this section. More importantly, these γ_k^ℓ computations specify that the antiparallel wave power will grow exponentially with an e -folding time of about 1 second. However, the empirical spectrum shows no evidence of secular exponential growth.

These disagreements point to the operation of a nonlinear saturation mechanism. Among other processes, the weak turbulence theory includes three-wave interactions [26]. They require that the matching conditions $k_a = k_b + k_c$ and $\omega_a = \omega_b + \omega_c$ be met by the three waves. Taken together, these conditions indicate

$$\frac{\omega_c}{k_c} = \frac{\omega_b - \omega_a}{k_b - k_a}. \quad (11)$$

Commonly analyzed so-called decay processes [27] involve the conversion of a high-frequency wave, say with label a , to a slightly lower frequency wave, b , of the same type along with a relatively low-frequency wave, c . For these processes, Eq. (11) indicates that the approximate group speed of waves a and b must equal the phase speed of wave c . If a and b are whistlers propagating along \vec{B}_0 , their group speed is roughly $v_{w,g} \approx 2v_{A,e} \sqrt{\omega/|\Omega_{ce}|}$, where $v_{A,e}$ is the electron

Alfvén speed. The low-frequency parallel-propagating candidate for wave c is the ion-acoustic wave [11]. In terms of the electron Alfvén speed, the ion-acoustic speed for an electron-proton plasma is approximately $v_{ia} \approx \sqrt{\beta m_e/m_p} v_{A,e}$, where β is the ratio of the particle pressure to the magnetic pressure, and m_p is the proton mass [17]. For the considered plasma with electron and proton temperatures $T_e \approx T_p \approx 10$ eV and densities $n_e \approx n_p \approx 6 \text{ cm}^{-3}$, this coefficient evaluates to $\sqrt{\beta m_e/m_p} \approx 0.03$, meaning strong interactions $v_{ia} \approx v_{w,g}$ between ion-acoustic waves and whistlers with frequencies $\omega > 0.01|\Omega_{ce}|$ are disallowed. More precisely, the ion-acoustic phase speed depends on the proton and electron equations of state, but $v_{ia}/v_{A,e} \approx \sqrt{\beta m_e/m_p}$ holds for all typical choices. Other three-wave processes that instead involve one whistler and two higher frequency waves are also likely to be insignificant in the weak turbulence framework [28].

4.2. Induced scattering

Another process described by the weak turbulence equations is induced scattering. The contribution $\tilde{\gamma}_k^{nl}$ to the nonlinear growth rate from this wave-wave-particle interaction is derived in Appendix A for a spectrum consisting of parallel-propagating whistler waves and is restated in Eq. (1). It is convenient to define a quantity $\tilde{s}_{k,k'}$ that consists of the wavenumber integrand of $\tilde{\gamma}_k^{nl} = \int \tilde{s}_{k,k'} \tilde{I}_+^B(k') dk'$ apart from the spectral density. For simplicity in notation, the tildes here, which denote use of normalized units, will be dropped in the remainder of this subsection.

This quantity $s_{k,k'}$ is both singular and oscillatory in the vicinity of $k' = k$. As a result, direct plots of it do not portray its features clearly. A plot of $S_{k,k''} \equiv \int_{k_\ell}^{k_u} s_{k,k'} dk'$ instead is presented in Fig. 3, specifically for $k = 0.352$. Computing $S_{k,k''}$ involves use of computer algebra software to expand Eq. (1) into a collection of terms with the form in Eq. (2) and evaluating these using fort-kv-ints. For each data point with wavenumber k'' in Fig. 3, the integral bounds k_ℓ and k_u are located halfway between k'' and the data points on either side of it. Equivalently, each data point is associated with its own region of wavenumber space centered on the point with a width $\Delta k'' = k_u - k_\ell$ equal to the data point spacing.

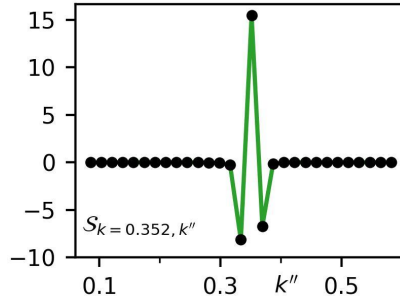


Figure 3: Coupling coefficient $S_{k=0.352,k''}$ between waves with wavenumbers $k = k''$ and $k = 0.352$. In the limit of closely spaced points, the nonlinear growth rate at wavenumber $k = 0.352$ is $\gamma_{k=0.352}^{nl} = \sum_{k''} S_{k=0.352,k''} I_+^B(k'')$.

Figure 3 shows that $S_{k,k''}$ for $k = 0.352$ is dominated by three extrema in the vicinity of $k'' = k$. For smaller $\Delta k''$, these peaks become more pronounced without bound, leading to the conclusion that $s_{k,k'}$ is oscillatory and singular at $k' = k$. The signs of the peaks indicate that waves with $k'' = 0.352$ promote their own growth while waves with slightly greater and slightly lesser wavenumbers dampen waves with $k = 0.352$. The net effect of the three extrema is to typically promote instability. Specifically, with $S_k \equiv \int_{k-(1.5)\Delta k''}^{k+(1.5)\Delta k''} s_{k,k'} dk' = \sum_{n=-1}^1 S_{k,k+n\Delta k''}$

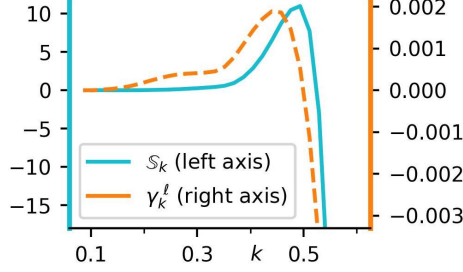


Figure 4: At wavenumber k , the linear growth rate γ_k^ℓ as well as a metric S_k of the nonlinear modification to the growth rate arising from waves with wavenumbers $k'' \approx k$. Specifically, $S_k = \sum_{j=-1}^1 S_{k,k+j\Delta k''}$, where $S_{k,k''}$ is described and plotted in Fig. 3 and $\Delta k''$ is the point spacing in that figure.

denoting the sum of the three peaks, $S_k > 0$ at $k = 0.352$. However, deviation from this general tendency can be brought about by variation in $I_+^B(k)$ in the vicinity of $k = 0.352$ that reduces the influence of the central peak.

Similar sets of three dominant extrema in $S_{k,k''}$ surrounding $k'' = k$ are seen for other k . In addition, as shown in the plot of S_k in Fig. 4, the sum of the three peaks has the same sign as the linear growth rate γ_k^ℓ at all k where $\gamma_k^\ell > 0$. This suggests that induced scattering may not be a viable process for stabilizing the spectrum.

4.3. Spectrum time evolution

Definitive assessment of the impact of induced scattering on a whistler spectrum $I_+^B(k)$ requires simulation of the wave kinetic equation. Driven by the nonlinear $\gamma_k^{n\ell}$ and the linear γ_k^ℓ growth rates, the spectrum evolves according to

$$\frac{dI_+^B(k)}{d(t|\Omega_{ce}|)} = 2I_+^B(k)(\gamma_k^\ell + \gamma_k^{n\ell}) = 2I_+^B(k)(\gamma_k^\ell + \int s_{k,k'} I_+^B(k') dk'). \quad (12)$$

Figure 5 presents a simulation of Eq. (12) using the γ_k^ℓ and $\gamma_k^{n\ell}$ calculations from LEOPARD and fort-kv-ints described above. For the initial conditions, $I_+^B(k)|_{t=0} = 1 \times 10^{-6}$ was adopted for all k , but the results do not substantially change if this value is increased or decreased by a factor of 10. For the time step, $|\Omega_{ce}|^{-1}$ was used, which balances computational efficiency with smoothness of the simulation in time.

The growth of the total wave power $\mathfrak{B}_{sim.} = 2 \int_{-\infty}^{\infty} I_+^B(k) dk$ in Fig. 5(a) is much slower than that predicted by linear theory. In particular, the exponential growth with e -folding time $\Delta t|\Omega_{ce}| = (2\gamma_k^\ell)^{-1} \sim 500$ predicted by linear theory between $k \approx 0.4$ and $k \approx 0.5$ corresponds to a wave power $\Delta \mathfrak{B}_{lin.} = 2I_+^B(k)|_{t=0} \Delta k \exp(20) \approx 100$ at $t|\Omega_{ce}| = 10^4$, which greatly exceeds the total power $\mathfrak{B}_{sim.}(t|\Omega_{ce}| = 10^4) \approx 4 \times 10^{-3}$ observed in the simulation. However, for almost the entire time interval displayed in Fig. 5(a), $\mathfrak{B}_{sim.}$ nonetheless greatly exceeds the empirical saturation wave power $\mathfrak{B}_{emp.} \approx 6 \times 10^{-5}$ presented above. This indicates that induced scattering cannot alone account for the stabilization of the instability observed by ARTEMIS.

Figure 5(b) shows that the distribution of wave power in k -space substantially differs in the simulation relative to what linear theory predicts. At early stages $t|\Omega_{ce}| \lesssim 4 \times 10^3$, the spectral density $I_+^B(k)$ is concentrated at $0.35 < k < 0.5$, where the linear growth rate γ_k^ℓ is the highest. However, at $t|\Omega_{ce}| = 8 \times 10^3$, the wave power is stronger at $k \approx 0.35$ than in regions $k \approx 0.45$

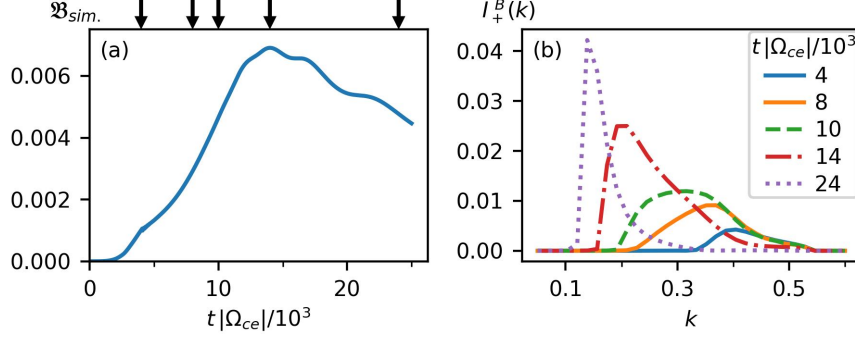


Figure 5: Overview of a whistler spectrum evolving according to the wave kinetic equation (12), which includes the linear growth rate γ_k^ℓ and a nonlinear growth rate γ_k^{nl} that describes induced scattering. Panel (a) presents the normalized total wave power $\mathfrak{B}_{sim.} = \langle |\vec{B}(\vec{r}, t)|^2 \rangle / B_0^2 = 2 \int_{-\infty}^{\infty} I_+^B(k) dk$. The power increases much more slowly than the exponential increase associated with the linear growth rate, but still starts to exceed the empirical wave power after $t|\Omega_{ce}| \sim 1000$. Panel (b) shows the wave spectrum $I_+^B(k)$ at the times marked with arrows above panel (a). As time goes on, wave power is transferred toward smaller wavenumbers.

of greater linear instability. This indicates that induced scattering transfers wave power toward smaller wavenumbers. This trend continues through $t|\Omega_{ce}| = 10 \times 10^3$, when $I_+^B(k)$ features a broad peak centered on the only weakly unstable wavenumber $k \approx 0.3$. Later, $I_+^B(k)$ develops a continuously narrowing and growing peak at progressively smaller and less linearly unstable wavenumbers, as shown at $t|\Omega_{ce}| = 14 \times 10^3$ and $t|\Omega_{ce}| = 24 \times 10^3$. This feature is almost certainly an artifact of the approximations adopted, such as the exclusion of three-wave interactions. The strength of the coupling between whistlers and ion-acoustic waves increases with decreasing whistler wavenumber, so including this coupling in future versions of the program will likely mitigate the spike at $k \approx 0.1$.

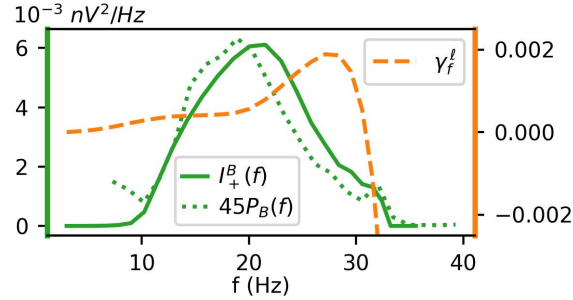


Figure 6: Comparison of the frequency dependence of the empirical spectral density $P_B(f)$, a simulated spectral density $I_+^B(f)$ derived from $I_+^B(k)$ in Fig. 5 at $t|\Omega_{ce}| = 8 \times 10^3$, and the linear growth rate γ_f^ℓ . The empirical and simulated spectral densities are correlated but differ in magnitude by a factor of approximately 45. The linear growth rate peaks at a frequency about 1.4 times higher than that at which the spectral densities peak.

Although the predicted and empirical total wave power are inconsistent, at some stages, the simulation does reproduce the frequency dependence of the observed spectrum $P_B(f)$. This is demonstrated in Fig. 6. Here, the Doppler-shifted spacecraft frame frequencies for γ_f^ℓ and $I_+^B(f)$

are given by $f(k) = (\omega(k) - v_{B_0}k)f_{ce}$, where $\omega(k)$ is the dispersion relation, v_{B_0} is the plasma speed projected onto \vec{B}_0 , and all quantities on the right hand side are in normalized units except f_{ce} . Also, the simulation output $I_+^B(k)$ at $t|\Omega_{ce}| = 8 \times 10^3$ is converted to a temporal frequency spectral density as $I_+^B(f) = 2B_0^2 I_+^B(k) / [(d\omega(k)/dk - v_{B_0})f_{ce}]$, where the prefactor $2B_0^2$ has been included so that $P_B(f) = I_+^B(f)$ can be expected.

Figure 6 shows that $I_+^B(f)$ and $P_B(f)$ are correlated throughout the whistler frequency band. On the other hand, the frequency of the maximum in γ_f^ℓ is greater than that of the maximum in $P_B(f)$ by a factor of 1.4, as mentioned previously. This means that the simulation of the instability might accurately depict a transfer of wave power toward smaller wavenumbers caused by induced scattering. However, the 1–2 orders of magnitude discrepancy between the total wave power of $I_+^B(f)$ and $P_B(f)$ disallows confidence in this conclusion.

5. Conclusions

Piecewise-analytical integration is a viable technique for evaluating one of the central expressions in the weak turbulence theory of parallel-propagating electromagnetic waves in a magnetized plasma. This double integral, describing induced scattering, features resonant denominators that are functions of both integrated variables: velocity v_\parallel and wavenumber k . Also appearing in the integrand are a particle velocity distribution function F and the wave spectral density I_+^B . When F and I_+^B are represented using splines in v_\parallel and k , the integrand becomes an analytically tractable rational function.

Partial fraction decomposition operations play a central role in computing the integral. Applying such operations with respect to v_\parallel allows this variable to be integrated over using elementary functions. Except in one case, this yields another rational function of k , but introduces high powers of k in the numerator and new poles in the denominator. As a consequence, the subsequent integral over k can typically be completed using standard techniques, but the extensiveness of the operations compels utilization of arbitrary precision arithmetic. When the k integrand is not a rational function, the integral can be expressed in terms of a special function, the dilogarithm.

In full, these computations yield values for the nonlinear growth rate $\gamma_k^{n\ell}$ at wavenumber k attributable to induced scattering. Simulating the evolution of a whistler wave spectrum that is influenced by $\gamma_k^{n\ell}$ reveals that induced scattering causes a transfer of wave power toward smaller wavenumbers. A spectrum of these electromagnetic waves measured in the solar wind by the spacecraft ARTEMIS also shows evidence of such transfer. However, the total wave power in this empirical spectrum is much less than that produced in simulations that include $\gamma_k^{n\ell}$, suggesting that the spectrum is influenced by additional nonlinear processes besides induced scattering.

These could be three-wave interactions. The associated nonlinear growth rates can be computed using similar strategies as employed for induced scattering. These computations will involve triple integrals with resonant denominators that are functions of the three integrated variables: wavenumber and two parallel velocities. Part of this calculation will have the form $\int (k - k_r)^{-1} \ln(k - k_j) \ln(k - k_m) dk$. Following manipulations of the integrand, such integrals can be expressed in terms of trilogarithm, dilogarithm, and logarithm functions [14]. However, as for the simpler dilogarithm and logarithm integrals needed for the induced scattering calculation, it will be necessary to track and correct for branch cut crossings introduced by the manipulations. Implementing this calculation constitutes a next step towards enabling complete simulations of the weak turbulence equations.

Appendix A. Induced scattering derivation

Below, the methods of [11] are used to derive the non-linear modification to the growth rate of parallel-propagating electromagnetic waves in a magnetized plasma caused by induced scattering. For simplicity, only one plasma species is considered, which is adequate for analysis of whistler waves with frequencies much greater than the proton gyrofrequency. From Eq. (10) of [11], the evolution of a particle velocity distribution function (vdf) in response to waves is governed for a magnetized plasma by

$$\left(-i\Omega\frac{\delta}{\delta\varphi} + \omega - \vec{k} \cdot \vec{v}\right)f_K = -\frac{ie}{m}\vec{E}_K^\top \vec{a}_K \nabla_v F(\vec{v}) - \frac{ie}{m}\nabla_v \cdot \int dK' \vec{a}_{K'}^\top \left[\vec{E}_{K'} f_{K-K'} - \langle \vec{E}_{K'} f_{K-K'} \rangle\right],$$

where \mathbb{I} is the identity matrix,

$$\vec{a}_K \equiv \left(1 - \frac{\vec{k} \cdot \vec{v}}{\omega}\right)\mathbb{I} + \frac{\vec{v}\vec{k}^T}{\omega},$$

$f_K(\vec{v})$ is the $K \equiv (\omega, k)$ Fourier component of the perturbation to the vdf caused by the waves, \vec{E}_K is the K Fourier component of the wave electric field, and $\int dK$ is shorthand for $\int d\omega dk$. With the waves taken to propagate along the background magnetic field $\vec{B}_0 = B_0 \hat{z}$,

$$f_K = \frac{1}{(2\pi)^2} \int f(z, t) e^{i(-kz + \omega t)} dz dt$$

and

$$\vec{E}_K = \frac{1}{(2\pi)^2} \int \vec{E}(z, t) e^{i(-kz + \omega t)} dz dt.$$

In addition, φ is the angle of \vec{v} in the plane perpendicular to \vec{B}_0 , and $F(\vec{v})$ is the homogeneous background particle vdf, normalized such that $\int F(\vec{v}) d\vec{v} = 1$. Further, $\Omega = eB_0/(mc)$ is the species gyrofrequency, and e and m are the species charge and mass.

In [11], a chain of equations is formed by writing $f_K = \sum_n f_K^{(N)}$, with term N going as $|\vec{E}|^N$. With attention restricted to electromagnetic modes, the linear term is

$$f_K^{(1)} = \left(E_K^+ e^{i\varphi} g_K^{-1} + E_K^- e^{-i\varphi} g_K^{+1}\right) T_K F(v_\parallel, v_\perp), \quad (\text{A.1})$$

where v_\parallel and v_\perp denote velocity parallel and perpendicular to \vec{B}_0 ,

$$T_K \equiv -\frac{ie}{m} \left(\frac{\omega - kv_\parallel}{\omega} \frac{\partial}{\partial v_\perp} + \frac{kv_\perp}{\omega} \frac{\partial}{\partial v_\parallel} \right),$$

and

$$g_K^M \equiv \frac{1}{\omega - kv_\parallel - M\Omega + i\epsilon},$$

where $i\epsilon$ is an infinitesimal imaginary part. Also, E_K^\pm are amplitudes defined by

$$E_K^\pm \equiv \frac{E_K^x \mp iE_K^y}{2}.$$

With the spectral densities I_K^\pm defined using $I_K^\pm \delta(K + K') \equiv \langle E_K^\pm E_{K'}^\mp \rangle$ [e.g., 29], where the angular brackets denote an ensemble average,

$$\langle |\vec{E}(z, t)|^2 \rangle = 2 \int_{-\infty}^{\infty} dk \int_{-\infty}^{\infty} d\omega (I_K^+ + I_K^-).$$

Also, $\langle E_K^+ E_{K'}^+ \rangle = 0$ and $\langle E_K^- E_{K'}^- \rangle = 0$ [26].

Analysis of induced scattering requires assessment of $f_K^{(3)}$. This is possible using Eq. (13) of [11], which expresses $f_K^{(N)}$ in terms of $f_K^{(N-1)}$, as well as Eq. (17) of [11], which states $f_K^{(2)}$. As argued in Sect. 4, it may be a reasonable approximation in an analysis of whistler spectra to ignore electrostatic modes. For this reason and for simplicity, the terms involving electrostatic fluctuations in Eq. (13) and Eq. (17) of [11] are dropped, which leads to

$$\begin{aligned} f_K^{(3)}(v_{\parallel}, v_{\perp}, \varphi) = & P \int dK' (1 - A) \left((E_{K'}^+ e^{i\varphi} + E_{K'}^- e^{-i\varphi}) T_{K'} - i D_{K'} (E_{K'}^+ e^{i\varphi} - E_{K'}^- e^{-i\varphi}) \frac{\partial}{\partial \varphi} \right) \\ & \frac{1}{2} \int dK_1 dK_2 \delta(K_1 + K_2 - (K - K')) \\ & \left(\sum_{+-} g_{K-K'}^0 [(T_{K_1} - D_{K_1}) g_{K_2}^{\mp 1} T_{K_2} + (T_{K_2} - D_{K_2}) g_{K_1}^{\pm 1} T_{K_1}] F(v_{\parallel}, v_{\perp}) (1 - A) E_{K_1}^{\mp} E_{K_2}^{\pm} + \right. \\ & \left. \sum_{+-} e^{\pm 2i\varphi} g_{K-K'}^{\mp 2} [(T_{K_1} + D_{K_1}) g_{K_2}^{\mp 1} T_{K_2} + (T_{K_2} + D_{K_2}) g_{K_1}^{\mp 1} T_{K_1}] F(v_{\parallel}, v_{\perp}) (1 - A) E_{K_1}^{\pm} E_{K_2}^{\mp} \right) \quad (\text{A.2}) \end{aligned}$$

where

$$D_K \equiv \frac{ie}{m} \frac{\omega - kv_{\parallel}}{\omega} \frac{1}{v_{\perp}},$$

and A is an averaging operator, satisfying $A(x) = \langle x \rangle$. In addition, P is an operator that solves $((\Omega/i)\partial/\partial\varphi + \omega - kv_{\parallel})f_K = H(\varphi)$ as $f_K = PH(\varphi)$. This operator satisfies $Pe^{iM\varphi} = e^{iM\varphi}g_K^{-M}$. For the remainder of this appendix, $f_K^{(2)}$ will be ignored because the modifications to the wave growth rate associated with it have already been derived in [11]. These describe mode coupling, which is argued in Sect. 4 to be subdominant to induced scattering for whistler spectra.

From Maxwell's equations,

$$\vec{E}_K \left(1 - \frac{c^2 k^2}{\omega^2} \right) = -\frac{4\pi i}{\omega} \vec{J}_K,$$

where $\vec{J}_K = en \int \vec{v} f_K(\vec{v}) d\vec{v}$ is the current density and n is the particle density. All terms of $f_K^{(1)}$ and $f_K^{(3)}$ in Eq. (A.1) and Eq. (A.2) have a sinusoidal φ dependence, so the parallel current $\sim \int d\vec{v} v_{\parallel} f(\vec{v})$ vanishes when integrated over azimuth. The perpendicular components satisfy

$$E_K^{\pm} \left(1 - \frac{c^2 k^2}{\omega^2} \right) = -\frac{4\pi i en}{\omega} \int v_{\pm} f_K d\vec{v}, \quad (\text{A.3})$$

where $v_{\pm} \equiv (v_x \mp iv_y)/2$.

Following [11], a wave kinetic equation can be derived by multiplying Eq. (A.3) by E_{-K}^{\mp} and taking an ensemble average. For the upper sign, the ensemble average is

$$\langle E_{-K}^- E_K^+ \rangle \left(1 - \frac{c^2 k^2}{\omega^2} \right) = -\frac{4\pi i en}{\omega} \left\langle E_{-K}^- \left[\int d\vec{v} v_+ f_K^{(1)} + \int d\vec{v} v_+ f_K^{(3)} \right] \right\rangle, \quad (\text{A.4})$$

and the lower sign leads to the same wave kinetic equation apart from the interchange $K \leftrightarrow -K$. By virtue of the form of the right hand side of Eq. (A.3), only terms of f_K with a $e^{+i\varphi}$ dependence on azimuth contribute to the current J_K^+ . From $f_K^{(3)}$, this includes one term proportional to $g_{K-K'}^0 E_{K'}^+ E_{K_1}^{\mp} E_{K_2}^{\pm}$ and another proportional to $g_{K-K'}^{-2} E_{K'}^- E_{K_1}^{\pm} E_{K_2}^{\mp}$.

In the random phase approximation, the ensemble average can be simplified using [26]

$$\begin{aligned}\langle E_{K_1} E_{K_2} E_{K_3} E_{K_4} \rangle = & I_{K_1} I_{K_3} \delta(K_1 + K_2) \delta(K_3 + K_4) + \\ & I_{K_1} I_{K_3} \delta(K_1 + K_4) \delta(K_3 + K_2) + \\ & I_{K_1} I_{K_2} \delta(K_1 + K_3) \delta(K_2 + K_4),\end{aligned}\quad (\text{A.5})$$

where the K shorthand has been temporarily extended to (k, ω, \pm) , and the delta functions enforce, e.g., $k_1 = -k_2$, $\omega_1 = -\omega_2$, and that K_1 and K_2 have opposite \pm signs. Equation (A.5) indicates that the terms in Eq. (A.2) proportional to $g_{K-K'}^{\mp 2}$ vanish under the ensemble averaging operation. The relevant ensemble average for the terms proportional to $g_{K-K'}^0$ is

$$\langle E_{-K}^- (1-A) E_{K'}^+ (1-A) E_{K_1}^\mp E_{K_2}^\pm \rangle = \begin{cases} \delta(-K + K_2) \delta(K_1 + K') & \text{for the upper sign} \\ \delta(-K + K_1) \delta(K' + K_2) & \text{for the lower sign.} \end{cases}$$

So, with $f_K = f_K^{(1)} + f_K^{(3)}$, multiplying Eq. (A.3) by E_{-K}^- and ensemble averaging yields

$$\begin{aligned}\Lambda_+(k, \omega) I_K^+ = & \frac{-4\pi^2 i e n}{\omega} I_K^+ \times \\ & \int dv_\perp dv_\parallel v_\perp^2 \int dK' g_K^{-1} T_{K'} g_{K-K'}^0 [(T_{-K'} - D_{-K'}) g_K^{-1} T_K + (T_K - D_K) g_{-K'}^{+1} T_{-K'}] F(v_\parallel, v_\perp) I_{K'}^+.\end{aligned}\quad (\text{A.6})$$

To lowest order in I_K^+ , the solution of Eq. (A.6) is $I_{k,\omega}^+ = I_+(k) \delta(\omega - \omega_k^+)$, where (k, ω_k^+) satisfies the dispersion relation, $\Lambda_+(k, \omega_k^+) = 0$ [29]. Here,

$$\Lambda_+(k, \omega) \equiv \epsilon_+(k, \omega) - \left(\frac{ck}{\omega} \right)^2,$$

where

$$\epsilon_+(k, \omega) \equiv 1 + \frac{4\pi^2 i e n}{\omega} \int dv_\perp dv_\parallel v_\perp^2 g_K^{-1} T_K F(v_\parallel, v_\perp)$$

is the dielectric constant.

Applying the prescription Eq. (34) from [11], inserting $I_{k,\omega}^+ = I_+(k) \delta(\omega - \omega_k^+)$, defining $K_+ \equiv (k, \omega_k^+)$, substituting the magnetic field spectral density $I_+^B(k) \equiv (ck/\omega_k^+)^2 I_+(k)$, and taking the imaginary part produces an expression for the time evolution of the wave spectrum

$$\begin{aligned}\frac{1}{2} \Lambda'_+(k, \omega_k^+) \frac{\partial}{\partial t} I_+^B(k) = & -\text{Im}(\Lambda_+(k, \omega_k^+)) I_+^B(k) - \frac{4\pi^2 e n}{\omega_k^+} I_+^B(k) \times \\ & \text{Im} \left[i \int dk' \left(\frac{\omega_{k'}^+}{k' c} \right)^2 \int dv_\perp dv_\parallel v_\perp^2 g_{K_+}^{-1} T_{K_+} g_{K_+-K'_+}^0 [(T_{-K'_+} - D_{-K'_+}) g_{K_+}^{-1} T_{K_+} + \right. \\ & \left. (T_{K_+} - D_{K_+}) g_{-K'_+}^{+1} T_{-K'_+}] F(v_\parallel, v_\perp) I_+^B(k') \right]\end{aligned}$$

where

$$\Lambda'_+(k, \omega) \equiv \frac{\partial \text{Re } \Lambda_+(k, \omega)}{\partial \omega}.$$

References

- [1] S. Kaplan, V. Tsytovich, Radio emission from beams of fast particles under cosmic conditions, *Soviet Astronomy*, Vol. 11, p. 956 11 (1968) 956.
- [2] D. B. Melrose, Collective plasma radiation processes, *Annual Review of Astronomy and Astrophysics* 29 (Volume 29, 1991) (1991) 31–57.
doi:<https://doi.org/10.1146/annurev.aa.29.090191.000335>.
URL <https://www.annualreviews.org/content/journals/10.1146/annurev.aa.29.090191.000335>
- [3] L. F. Ziebell, P. H. Yoon, L. T. Petruzzellis, R. Gaelzer, J. Pavan, Plasma emission by nonlinear electromagnetic processes, *The Astrophysical Journal* 806 (2) (2015) 237.
doi:10.1088/0004-637X/806/2/237.
URL <https://dx.doi.org/10.1088/0004-637X/806/2/237>
- [4] M. Mithaiwala, L. Rudakov, G. Ganguli, C. Crabtree, Weak turbulence theory of the nonlinear evolution of the ion ring distribution, *Physics of Plasmas* 18 (5) (2011) 055710. arXiv:https://pubs.aip.org/aip/pop/article-pdf/doi/10.1063/1.3574389/15957380/055710_1_online.pdf, doi:10.1063/1.3574389.
URL <https://doi.org/10.1063/1.3574389>
- [5] L. Rudakov, M. Mithaiwala, G. Ganguli, C. Crabtree, Linear and nonlinear Landau resonance of kinetic Alfvén waves: Consequences for electron distribution and wave spectrum in the solar wind, *Physics of Plasmas* 18 (1) (2011) 012307. doi:10.1063/1.3532819.
URL <http://dx.doi.org/10.1063/1.3532819>
- [6] B. D. Fried, S. D. Conte, *The plasma dispersion function: the Hilbert transform of the Gaussian*, Academic press, 2015.
- [7] D. J. Percival, P. A. Robinson, Generalized plasma dispersion functions, *Journal of Mathematical Physics* 39 (7) (1998) 3678–3693. arXiv:https://pubs.aip.org/aip/jmp/article-pdf/39/7/3678/19028219/3678_1_online.pdf, doi:10.1063/1.532460.
URL <https://doi.org/10.1063/1.532460>
- [8] B. Layden, I. H. Cairns, P. A. Robinson, D. J. Percival, Exact evaluation of the quadratic longitudinal response function for an unmagnetized Maxwellian plasma, *Physics of Plasmas* 19 (7) (2012) 072308. arXiv:https://pubs.aip.org/aip/pop/article-pdf/doi/10.1063/1.4737603/16112925/072308_1_online.pdf, doi:10.1063/1.4737603.
URL <https://doi.org/10.1063/1.4737603>
- [9] P. Astfalk, F. Jenko, Leopard: A grid-based dispersion relation solver for arbitrary gyrotropic distributions, *Journal of Geophysical Research: Space Physics* 122 (1) (2017) 89–101. arXiv:<https://agupubs.onlinelibrary.wiley.com/doi/pdf/10.1002/2016JA023522>, doi:<https://doi.org/10.1002/2016JA023522>.
URL <https://agupubs.onlinelibrary.wiley.com/doi/abs/10.1002/2016JA023522>
- [10] P. Astfalk, F. Jenko, On the quasi-linear saturation of the parallel proton firehose instability using a full-f approach, *Journal of Geophysical Research: Space Physics* 123 (9) (2018) 7153–7166. arXiv:<https://agupubs.onlinelibrary.wiley.com/doi/pdf/10.1029/2017JA025143>,

doi:<https://doi.org/10.1029/2017JA025143>.

URL <https://agupubs.onlinelibrary.wiley.com/doi/abs/10.1029/2017JA025143>

- [11] P. H. Yoon, Kinetic theory of hydromagnetic turbulence. i. formal results for parallel propagation, *Physics of Plasmas* 14 (10) (2007) 102302. arXiv:https://pubs.aip.org/aip/pop/article-pdf/doi/10.1063/1.2780139/15763964/102302_1_online.pdf, doi:10.1063/1.2780139. URL <https://doi.org/10.1063/1.2780139>
- [12] C. Lacombe, O. Alexandrova, L. Matteini, O. Santolík, N. Cornilleau-Wehrin, A. Mangeney, Y. de Conchy, M. Maksimovic, Whistler mode waves and the electron heat flux in the solar wind: Cluster observations, *The Astrophysical Journal* 796 (1) (2014) 5. doi:10.1088/0004-637X/796/1/5. URL <https://dx.doi.org/10.1088/0004-637X/796/1/5>
- [13] Y. Tong, I. Y. Vasko, A. V. Artemyev, S. D. Bale, F. S. Mozer, Statistical study of whistler waves in the solar wind at 1 au, *The Astrophysical Journal* 878 (1) (2019) 41. doi:10.3847/1538-4357/ab1f05. URL <https://dx.doi.org/10.3847/1538-4357/ab1f05>
- [14] L. Lewin, *Polylogarithms and Associated Functions*, North Holland, 1981.
- [15] Y. Ma, J. Yu, Y. Wang, Efficient recursive methods for partial fraction expansion of general rational functions, *Journal of Applied Mathematics* 2014 (1) (2014) 895036. arXiv:<https://onlinelibrary.wiley.com/doi/pdf/10.1155/2014/895036>, doi:<https://doi.org/10.1155/2014/895036>. URL <https://onlinelibrary.wiley.com/doi/abs/10.1155/2014/895036>
- [16] R. L. Stenzel, Whistler waves in space and laboratory plasmas, *Journal of Geophysical Research: Space Physics* 104 (A7) (1999) 14379–14395. arXiv:<https://agupubs.onlinelibrary.wiley.com/doi/pdf/10.1029/1998JA900120>, doi:<https://doi.org/10.1029/1998JA900120>. URL <https://agupubs.onlinelibrary.wiley.com/doi/abs/10.1029/1998JA900120>
- [17] T. H. Stix, *Waves in Plasmas*, American Institute of Physics, 1992.
- [18] V. Angelopoulos, *The ARTEMIS Mission*, Springer New York, 2010, p. 3–25. doi:10.1007/978-1-4614-9554-3_2. URL http://dx.doi.org/10.1007/978-1-4614-9554-3_2
- [19] D. Stansby, T. S. Horbury, C. H. K. Chen, L. Matteini, Experimental determination of whistler wave dispersion relation in the solar wind, *The Astrophysical Journal Letters* 829 (1) (2016) L16. doi:10.3847/2041-8205/829/1/L16. URL <https://dx.doi.org/10.3847/2041-8205/829/1/L16>
- [20] A. Roux, O. Le Contel, C. Coillot, A. Bouabdellah, B. de la Porte, D. Alison, S. Ruocco, M. C. Vassal, The search coil magnetometer for THEMIS, *Space Science Reviews* 141 (1–4) (2008) 265–275. doi:10.1007/s11214-008-9455-8. URL <http://dx.doi.org/10.1007/s11214-008-9455-8>

- [21] H. U. Auster, K. H. Glassmeier, W. Magnes, O. Aydogar, W. Baumjohann, D. Constantinescu, D. Fischer, K. H. Fornacon, E. Georgescu, P. Harvey, O. Hillenmaier, R. Kroth, M. Ludlam, Y. Narita, R. Nakamura, K. Okrafka, F. Plaschke, I. Richter, H. Schwarzl, B. Stoll, A. Valavanoglou, M. Wiedemann, The THEMIS fluxgate magnetometer, *Space Science Reviews* 141 (1–4) (2008) 235–264. doi:10.1007/s11214-008-9365-9.
URL <http://dx.doi.org/10.1007/s11214-008-9365-9>
- [22] O. Santolík, M. Parrot, F. Lefeuvre, Singular value decomposition methods for wave propagation analysis, *Radio Science* 38 (1) (2003) 10–1–10–13. doi:10.1029/2000RS002523.
- [23] J. W. Bonnell, F. S. Mozer, G. T. Delory, A. J. Hull, R. E. Ergun, C. M. Cully, V. Angelopoulos, P. R. Harvey, The Electric Field Instrument (EFI) for THEMIS, Springer New York, 2009, p. 303–341. doi:10.1007/978-0-387-89820-9_14.
URL http://dx.doi.org/10.1007/978-0-387-89820-9_14
- [24] J. P. McFadden, C. W. Carlson, D. Larson, M. Ludlam, R. Abiad, B. Elliott, P. Turin, M. Marckwordt, V. Angelopoulos, The THEMIS ESA plasma instrument and in-flight calibration, *Space Science Reviews* 141 (1–4) (2008) 277–302. doi:10.1007/s11214-008-9440-2.
URL <http://dx.doi.org/10.1007/s11214-008-9440-2>
- [25] B. Page, I. Y. Vasko, A. V. Artemyev, S. D. Bale, Generation of high-frequency whistler waves in the earth’s quasi-perpendicular bow shock, *The Astrophysical Journal Letters* 919 (2) (2021) L17. doi:10.3847/2041-8213/ac2748.
URL <https://dx.doi.org/10.3847/2041-8213/ac2748>
- [26] R. C. Davidson, *Methods in Nonlinear Plasma Theory*, Pure and Applied Physics, Academic Press, 1972.
- [27] V. N. Tsytovich, *Nonlinear Effects in Plasma*, Springer New York, NY, 1970. doi:10.1007/978-1-4684-1788-3.
- [28] D. Melrose, Three-wave interactions involving one whistler, *Australian Journal of Physics* 28 (1) (1975) 101. doi:10.1071/ph750101.
URL <http://dx.doi.org/10.1071/PH750101>
- [29] B. B. Kadomtsev, *Plasma Turbulence*, Academic Press, 1965.